Energy Conversion and Management 226 (2020) 113550

Contents lists available at ScienceDirect

Energy Conversion and Management

journal homepage: www.elsevier.com/locate/enconman

Kinetic parameters estimation via dragonfly algorithm (DA) and comparison of cylindrical and spherical reactors performance for CO_2 hydrogenation to hydrocarbons

Sara Najari [a], Samrand Saeidi [b,*], Gyula Gróf [a], Frerich J. Keil [c], Alírio E. Rodrigues [d]

[a] Department of Energy Engineering, Faculty of Mechanical Engineering, Budapest University of Technology and Economics, Budapest, Hungary
[b] Institute of Energy and Process Systems Engineering, Technische Universität Braunschweig, Franz-Liszt-Str. 35, 38106 Braunschweig, Germany
[c] Institute of Chemical Reaction Engineering, Hamburg University of Technology, Hamburg D-21073, Germany
[d] Laboratory of Separation and Reaction Engineering – Laboratory of Catalysis and Materials (LSRE-LCM), Associate Laboratory LSRE-LCM, Faculdade de Engenharia, Universidade do Porto, Rua Dr. Roberto Frias, 4200-465 Porto, Portugal

ARTICLE INFO

Keywords:
CO_2 hydrogenation
Optimization
DA algorithm
Cylindrical reactor
Axial and radial flow spherical reactor

ABSTRACT

Climate change and global warming, as well as growing global demand for hydrocarbons in industrial sectors, make great incentives to investigate the utilization of CO_2 for hydrocarbons production. Therefore, finding an in-depth understanding of the CO_2 hydrogenation reactors along with simulating reactor responses to different operating conditions are of paramount importance. However, the reaction mechanisms for CO_2 hydrogenation and their corresponding kinetic parameters have been disputable yet. In this regard, considering the previously proposed Langmuir-Hinshelwood-Hougen-Watson (LHHW) mechanism, which considered CO_2 hydrogenation as a combination of reverse water gas shift (RWGS) and Fischer-Tropsch (FT) reactions, and using a one-dimensional pseudo-homogeneous non-isothermal model, kinetic parameters of the rate expressions are estimated via fitting experimental and modelling data through a novel swarm intelligence optimization technique called dragonfly algorithm (DA). The predicted reactants conversion using DA algorithm are closer to the experimental data (with about 4% error) comparing to those obtained by the artificial bee colony (ABC) algorithm, and are in significant agreement with available literature data. The proposed model is used to assess the effect of reactor configuration on the performance and temperature fluctuations. Results show that axial flow spherical reactor (AFSR) and radial flow spherical reactor (RFSR) exhibiting the same surface area with that of the cylindrical reactor (CR), i.e., AFSR-2 and RFSR-2-i are the most efficient exhibiting hydrocarbons selectivity of 40.330% and 40.286% at CO_2 conversion of 53.763% and 53.891%. In addition, it is revealed that the location of the jacket has an essential role in controlling the reactor temperature.

1. Introduction

Environmental issues regarding CO_2 emissions along with diminishing fossil fuels as the primary feedstock for the production of various chemicals have made great motivations to use CO_2 as a source of hydrocarbons and chemicals production [1–5]. Despite some progress in this field, establishing efficient and competitive methods of CO_2 hydrogenation to produce added-value chemicals has yet remained a challenging issue [6,7]. In fact, since CO_2 is thermodynamically stable, its activation is not easy and requires high energy [8,9]. On the other hand, H_2, which is a high-energy molecule, can be used as a proper substance for CO_2 activation and transformation. Various sources of H_2 include fossil fuels [10–14], water splitting and biomass gasification [15], and renewable sources are available [16,17]. However, appropriate operating conditions and reactor configurations for CO_2 hydrogenation to hydrocarbons [18–21] along with effective catalysts [22–27] need to be developed.

Modeling and simulation of chemical processes are effective tools to gain insight about the reactor performance at various conditions (changes in configurations and operating conditions) [28–37]. In addition, the estimation of kinetic parameters is of significant importance in reactor modeling and design [38–43]. To this end, the mechanism of CO_2 hydrogenation and rate expressions are a prerequisite [44].

* Corresponding author at: Institute of Energy and Process Systems Engineering, Technische Universität Braunschweig, Franz-Liszt-Str. 35, 38106 Braunschweig, Germany.
E-mail address: samrandsaidi@gmail.com (S. Saeidi).

https://doi.org/10.1016/j.enconman.2020.113550
Received 6 August 2020; Received in revised form 10 October 2020; Accepted 12 October 2020
Available online 25 October 2020

Nomenclature

A_C	cross sectional area of CR [m^2]
A_r	surface area of RFSR [m^2]
A_z	surface area of AFSR [m^2]
a_{j,H_2O}	inhibition coefficient for H_2O in the j-th reaction [–]
b_{j,CO_2}	inhibition coefficient for CO_2 in the j-th reaction [–]
C_{pg}	specific heat of the gas mixture in the reactor [J mol^{-1} K^{-1}]
C_i	concentration of the i-th component [mol m^{-3}]
C_t	total concentration of the reactor mixture [mol m^{-3}]
D_c	diameter of CR [m]
D_p	particle diameter [m]
E_j	apparent activation energy of the j-th reaction [kJ mol^{-1}]
f_s	correction factor [–]
h_r	heat transfer coefficient of the reactor [Wm^{-2} K^{-1}]
K_{eq}	equilibrium constant of the shift reaction [–]
K_g	thermal conductivity of gas mixture in the reactor [Wm^{-1} K^{-1}]
K_w	thermal conductivity of reactor wall [Wm^{-1} K^{-1}]
k_j	pre-exponential factor in Arrhenius law for the j-th reaction [mol $s^{-1}g^{-1}MPa^{-1}$]
K_j	reaction rate coefficient for the j-th reaction [mol $s^{-1}g^{-1}MPa^{-1}$]
L	reactor length [m]
m_{cat}	catalyst weight [g]
Mw	molecular weight [g/mol]
P	reactor pressure [Pa]
R	universal gas constant [J $mol^{-1}K^{-1}$]
Re	Reynolds number [–]
r_j	rate for the j-th reaction [mol g_{cat}^{-1} s^{-1}]
r	radius of RFSR [m]
r_z	radius of AFSR at each z [m]
R_z	radius of AFSR [m]
T	temperature of gas mixture in the reactor [K]
T_j	temperature of jacket [K]
U_c	overall heat transfer coefficient between jacket and CR [Wm^{-2} K^{-1}]
U_z	overall heat transfer coefficient between jacket and AFSR [Wm^{-2} K^{-1}]
U_r	overall heat transfer coefficient between jacket and RFSR [Wm^{-2} K^{-1}]
u_c	velocity of gas mixture in CR [m s^{-1}]
u_z	velocity of gas mixture in AFSR [m s^{-1}]
u_r	velocity of gas mixture in RFSR [m s^{-1}]
V_s	volumetric flow rate at reactor condition [m^3 s^{-1}]
S_i	Sutherland constant of pure component "i" [K]
S_{ij}	geometric mean of S_i and S_j [K]
z	axial dimension [m]

Greek letters

μ_g	viscosity of gas mixture in the reactor [kg m^{-1} s^{-1}]
ρ_g	density of gas mixture in the reactor [kg m^{-3}]
ΔH_{fj}	enthalpy of formation for the j-th reaction [J mol^{-1}]
ρ_B	density of catalytic bed [g m^{-3}]
ρ_p	density of catalyst particles [g m^{-3}]
ε_b	bed porosity [–]
θ_{ij}	constant parameter in Eq. (A-4) [–]
ϕ_{ij}	constant parameter in Eq. (A-7) [–]

However, few kinds of research have been devoted to assessing the kinetics of the CO_2 hydrogenation to added-value chemicals after the pioneering research of Riedel et al. [45]. Considering propylene as the main product over K/Fe-Al_2O_3, kinetic parameters of the corresponding rate expressions for the reverse water gas shift (RWGS), Fischer-Tropsch (FT) and direct hydrogenation of CO_2 were estimated via fitting the calculated and experimental data by regression using DATA FIT and ASPEN HYSYS [45]. Using these kinetic data, Willauer et al. [46] considered methane as another product over Al_2O_3-supported K/Mn/Fe and calculated the corresponding kinetic parameters via fitting the computational and experimental results using the COMSOL package. However, Kirsch et al. [47] proposed a power-to-fuel process via integrating RWGS reactor, FT reactor and hydrocracking (HC). For the RWGS the reactor, outputs were calculated based on the minimization of the Gibbs enthalpy, while for the FT and HC reactors, the kinetic rate expressions were used from the data provided by Sun et al. [48]. The modeling was performed using Simulink in the MATLAB environment to assess the effect of different configurations on the production of C_{10}-C_{20} liquid hydrocarbons. Recently, Do and Kim [49] used the calculated kinetic parameters of Najari et al. [50] and developed a novel process for the production of C_2-C_4 hydrocarbons from CO_2 hydrogenation using ASPEN Plus V10. In the proposed scheme, membrane, PSA, absorption and distillation were used as separation methods. Besides, heat and power plants were integrated to obtain an efficient and economical process. However, novel optimization algorithms are required for practical applications, due to the required precision in determining the kinetic parameters.

In our previous study [50], we proposed methane, ethylene, ethane, propylene, propane, butylene and *iso*-butane as the products of CO_2 hydrogenation process, and the proposed reaction rates of Saeidi et al. [44], based on the LHHW mechanism, were used. The kinetic parameters were calculated by fitting the experimental and calculated data through artificial bee colony (ABC) and differential evolution (DE) optimization algorithms, which were solved employing MATLAB programming software. The results revealed that ABC algorithm was able to provide more appropriate estimations compared to those of DE [50]. In fact, ABC is a swarm intelligence (SI)-based algorithm, which saves information of search space in contrast to other algorithms. In addition, SI-based algorithms are very flexible and can be used for a variety of optimization problems. However, the estimated kinetic parameters using ABC algorithm overestimated the reactant conversions.

Accordingly, a newly developed heuristic SI-based optimization algorithm, dragonfly algorithm (DA), is used in the present study to estimate kinetic parameters of the previously proposed LHHW-based rate expressions through fitting the experimental with modeling data. The prediction results are compared to available literature data. In addition, employing the proposed model, the influence of reactor configuration is assessed. To this end, the performance of axial flow spherical reactor (AFSR) and radial flow spherical reactor (RFSR) are compared to that of cylindrical reactor (CR) in terms of reactants conversion and products distribution. Moreover, the role of jacket position is investigated on the temperature of the spherical reactors.

2. Mathematical modeling

The mathematical modeling of the fixed-bed reactors is

Table 1
Reactions and proposed rate equations [44].

Reactions			Rate equations
Shift	$CO_2+H_2 \leftrightarrow CO + H_2O$	Forward	$r_1 = K_1 \frac{P_{CO_2}P_{H_2}}{P_{CO} + a_{1,H_2O}P_{H_2O} + b_{1,CO_2}P_{CO_2}}$
		Backward	$r_9 = K_9 \frac{P_{CO}P_{H_2O}/K_{eq}}{P_{CO} + a_{9,H_2O}P_{H_2O} + b_{9,CO_2}P_{CO_2}}$
			$log(K_{eq}) = (\frac{B_1}{T} - B_2)$
FT	$CO+3H_2 \rightarrow CH_4 + H_2O$		$r_2 = K_2 \frac{P_{CO}P_{H_2}}{P_{CO} + a_{2,H_2O}P_{H_2O} + b_{2,CO_2}P_{CO_2}}$
	$2CO+4H_2 \rightarrow C_2H_4 + 2H_2O$		$r_3 = K_3 \frac{P_{CO}P_{H_2}}{P_{CO} + a_{3,H_2O}P_{H_2O} + b_{3,CO_2}P_{CO_2}}$
	$2CO+5H_2 \rightarrow C_2H_6 + 2H_2O$		$r_4 = K_4 \frac{P_{CO}P_{H_2}}{P_{CO} + a_{4,H_2O}P_{H_2O} + b_{4,CO_2}P_{CO_2}}$
	$3CO+6H_2 \rightarrow C_3H_6 + 3H_2O$		$r_5 = K_5 \frac{P_{CO}P_{H_2}}{P_{CO} + a_{5,H_2O}P_{H_2O} + b_{5,CO_2}P_{CO_2}}$
	$3CO+7H_2 \rightarrow C_3H_8 + 3H_2O$		$r_6 = K_6 \frac{P_{CO}P_{H_2}}{P_{CO} + a_{6,H_2O}P_{H_2O} + b_{6,CO_2}P_{CO_2}}$
	$4CO+8H_2 \rightarrow C_4H_8 + 4H_2O$		$r_7 = K_7 \frac{P_{CO}P_{H_2}}{P_{CO} + a_{7,H_2O}P_{H_2O} + b_{7,CO_2}P_{CO_2}}$
	$4CO+9H_2 \rightarrow C_4H_{10} + 4H_2O$		$r_8 = K_8 \frac{P_{CO}P_{H_2}}{P_{CO} + a_{8,H_2O}P_{H_2O} + b_{8,CO_2}P_{CO_2}}$

accomplished considering the following assumptions:

1. One-dimensional pseudo-homogeneous plug flow reactor
2. Conductive heat transfer is considered to be negligible compared to convective heat transfer
3. The physical properties and reaction enthalpy are temperature dependent
4. Gases are considered as the ideal gas
5. Steady-state conditions
6. Jacket temperature is considered constant

The reactions and the rate expressions are presented in Table 1.

The reaction rate coefficients, K_j, can be calculated via Arrhenius expression as follows:

$$K_j = k_j exp\left(-\frac{E_j}{RT}\right) \quad (1)$$

where k_j and E_j are the pre-exponential factor and activation energy of the j-th reaction, R is the universal gas constant, and T is the absolute temperature. Accordingly, the rate of each component, which are used in the modeling, can be written as follows (Eq. (2) to Eq. (12)):

$$r_{H_2} = -(\eta_1 r_1 + 3\eta_2 r_2 + 4\eta_3 r_3 + 5\eta_4 r_4 + 6\eta_5 r_5 + 7\eta_6 r_6 + 8\eta_7 r_7 + 9\eta_8 r_8 - \eta_9 r_9) \quad (2)$$

$$r_{CO_2} = -(\eta_1 r_1 - \eta_9 r_9) \quad (3)$$

$$r_{CO} = \eta_1 r_1 - \eta_2 r_2 - 2\eta_3 r_3 - 2\eta_4 r_4 - 3\eta_5 r_5 - 3\eta_6 r_6 - 4\eta_7 r_7 - 4\eta_8 r_8 - \eta_9 r_9 \quad (4)$$

$$r_{CH_4} = \eta_2 r_2 \quad (5)$$

$$r_{C_2H_4} = \eta_3 r_3 \quad (6)$$

$$r_{C_2H_6} = \eta_4 r_4 \quad (7)$$

$$r_{C_3H_6} = \eta_5 r_5 \quad (8)$$

$$r_{C_3H_8} = \eta_6 r_6 \quad (9)$$

$$r_{C_4H_8} = \eta_7 r_7 \quad (10)$$

$$r_{C_4H_{10}} = \eta_8 r_8 \quad (11)$$

$$r_{H_2O} = \eta_1 r_1 + \eta_2 r_2 + 2\eta_3 r_3 + 2\eta_4 r_4 + 3\eta_5 r_5 + 3\eta_6 r_6 + 4\eta_7 r_7 + 4\eta_8 r_8 - \eta_9 r_9 \quad (12)$$

where r_j is the rate of j-th reaction and η_j is the corresponding effectiveness factor [20].

2.1. Cylindrical (tubular) reactor

The species mass and energy balances are represented by Eq. (13) and Eq. (14) and momentum balance across the CR is expressed using Ergun equation (Eq. (15)).

$$\frac{dC_i}{dz} = \frac{1}{u_c}\rho_p(1-\varepsilon_b)r_i \quad (13)$$

$$\frac{dT}{dz} = \frac{1}{C_t C_{pg} u_c}\left(\sum_{j=1}^{9}\rho_p(1-\varepsilon_b)r_j(-\Delta H_{f,j}) + \frac{4U_C}{D_c}(T_j - T) - C_{pg}u_c T\frac{dC_t}{dz}\right) \quad (14)$$

$$\frac{dP}{dz} = -\left[150\frac{(1-\varepsilon_b)^2\mu_g V_s}{\varepsilon_b{}^3 d_p{}^2 A_c} + 1.75\frac{(1-\varepsilon_b)\rho_g V_s^2}{\varepsilon_b{}^3 d_p A_c{}^2}\right] \quad (15)$$

where C_i (i = CO_2, H_2, CO, CH_4, C_2H_4, C_2H_6, C_3H_6, C_3H_8, C_4H_8, C_4H_{10}, H_2O) and C_t are the concentration of species i and total concentration in the reactor, and r_i are represented in Eq. (2) to Eq. (12). ρ_p is the density of catalyst particles and ε_b is the void fraction in the bed. T, T_j and P are the reactor temperature, jacket temperature and reactor pressure, respectively. In addition, D_c and A_c are the diameter and cross-sectional area of the cylindrical reactor, while U_C is the heat transfer coefficient between jacket and CR. u_c and V_s are velocity in CR and volumetric flow rate.

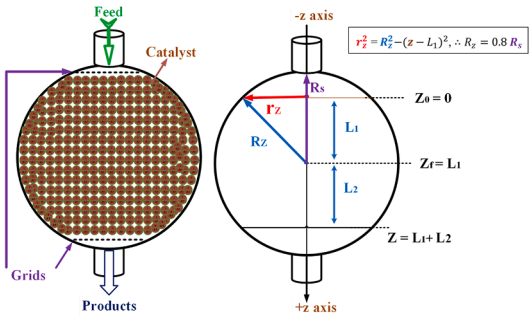

Fig. 1. Schematics of axial flow spherical reactor (AFSR).

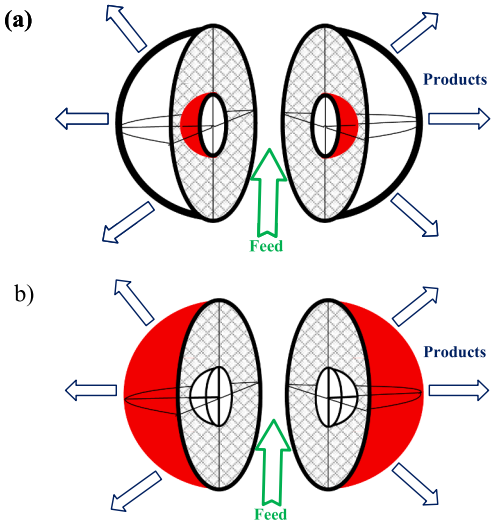

Fig. 2. Schematics of radial flow spherical reactor (RFSR) with a) inside jacket and b) outside jacket. (The radii of the inner and outer spheres are R_i and R_o, respectively and $R_i = 0.2\ R_o$).

2.2. Axial spherical reactor

In this configuration, feed is introduced from the top of the reactor. Since the entrance and outlet have a small cross sectional area, which may cause a considerable pressure drop, two grids are used to hold the catalysts near the inlet and outlet of the reactor as illustrated in Fig. 1.

The species balance, heat balance and pressure drop across the AFSR are represented in Eq. (16), Eq. (17) and Eq. (18). In this configuration, the cross sectional area changes with length, i.e. z, as can be observed in Eq. (19).

$$\frac{dC_i}{dz} = \frac{1}{u_z}\left[\rho_p(1-\varepsilon_b)r_i - \frac{C_i}{A_z}\left(A_z\frac{du_z}{dz} + u_z\frac{dA_z}{dz}\right)\right] \tag{16}$$

$$\frac{dT}{dz} = \frac{1}{C_t C_{pg} u_z}\left(\sum_{j=1}^{9}\rho_p(1-\varepsilon_b)r_j(-\Delta H_{fj}) + \frac{2\pi r_z U_z}{A_z}(T_j - T) - \frac{C_{pg}}{A_z}\left(u_z A_z T\frac{dC_t}{dz} + C_t T\frac{d(A_z u_z)}{dz}\right)\right) \tag{17}$$

$$\frac{dP}{dz} = -\left[150\frac{(1-\varepsilon_b)^2\mu_g V_s}{\varepsilon_b{}^3 d_p{}^2 A_z} + 1.75\frac{(1-\varepsilon_b)\rho_g V_s^2}{\varepsilon_b{}^3 d_p A_z{}^2}\right] \tag{18}$$

$$A_z = \pi\left[R_z{}^2 - (z-L_1)^2\right];\ \ L_1 = L_2 \tag{19}$$

$$u_z = \frac{V_s}{\varepsilon_b A_z} \tag{20}$$

where r_z and A_z are the radius and cross-sectional area of the AFSR, while U_z is the heat transfer coefficient between jacket and AFSR. u_z and V_s are velocity in AFSR and volumetric flow rate. The geometries of the AFSR have been provided in Fig. 1, and thus the radius and surface area of the reactor can be calculated via the information in Fig. 1 and Eq. (19), respectively.

2.3. Radial spherical reactor

In this configuration, feed is assumed to enter from the center of the reactor and two possibilities for the jacket location (inside and outside) are considered as illustrated in Fig. 2 (a) and Fig. 2 (b).

The species balance, heat balance and pressure drop across the AFSR are represented in Eq. (21), Eq. (22) and Eq. (23). In this configuration,

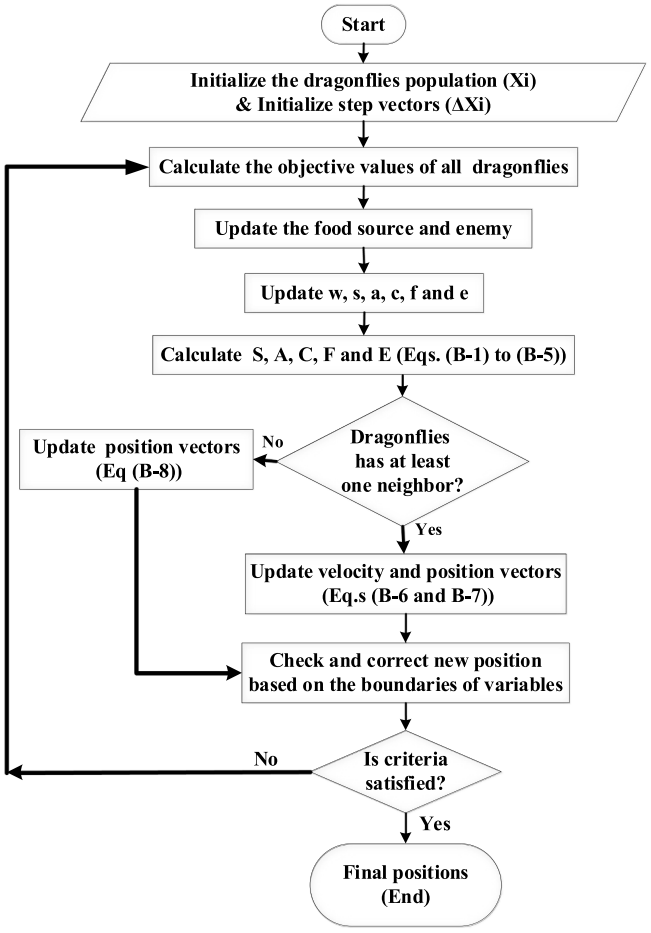

Fig. 3. Dragonfly algorithm flowchart [52].

the cross sectional area changes with diameter, i.e. r, as can be observed in Eq. (24).

$$\frac{dC_i}{dr} = \frac{1}{u_r}\left[\rho_p(1-\varepsilon_b)r_i - \frac{C_i}{A_r}\left(A_r\frac{du_r}{dr} + u_r\frac{dA_r}{dr}\right)\right] \tag{21}$$

$$\frac{dT}{dr} = \frac{1}{C_t C_{pg} u_r}\left(\sum_{j=1}^{9}\rho_p(1-\varepsilon_b)r_j(-\Delta H_{fj}) + \frac{8\pi r U_r}{A_r}(T_j - T) - \frac{C_{pg}}{A_r}\left(u_r A_r T\frac{dC_t}{dr} + C_t T\frac{d(A_r u_r)}{dr}\right)\right) \tag{22}$$

$$\frac{dP}{dr} = -\left[150\frac{(1-\varepsilon_b)^2\mu_g V_s}{\varepsilon_b{}^3 d_p{}^2 A_r} + 1.75\frac{(1-\varepsilon_b)\rho_g V_s{}^2}{\varepsilon_b{}^3 d_p A_r{}^2}\right] \tag{23}$$

$$A_r = 4\pi r^2 \tag{24}$$

$$u_r = \frac{V_s}{\varepsilon_b A_r} \tag{25}$$

where r and A_r are the radius and cross-sectional area of the RFSR, while U_r is the heat transfer coefficient between jacket and RFSR and u_r is velocity in RFSR. In addition, for RFSR the surface area can be calculated via the information in Fig. 2 and Eq. (24). The required correlations and auxiliary equations are presented in Appendix A.

3. Dragonfly algorithm

A version of so-called SI algorithms [51], namely a dragonfly algorithm (DA) [52] is used to optimize the kinetic parameters. Efficient

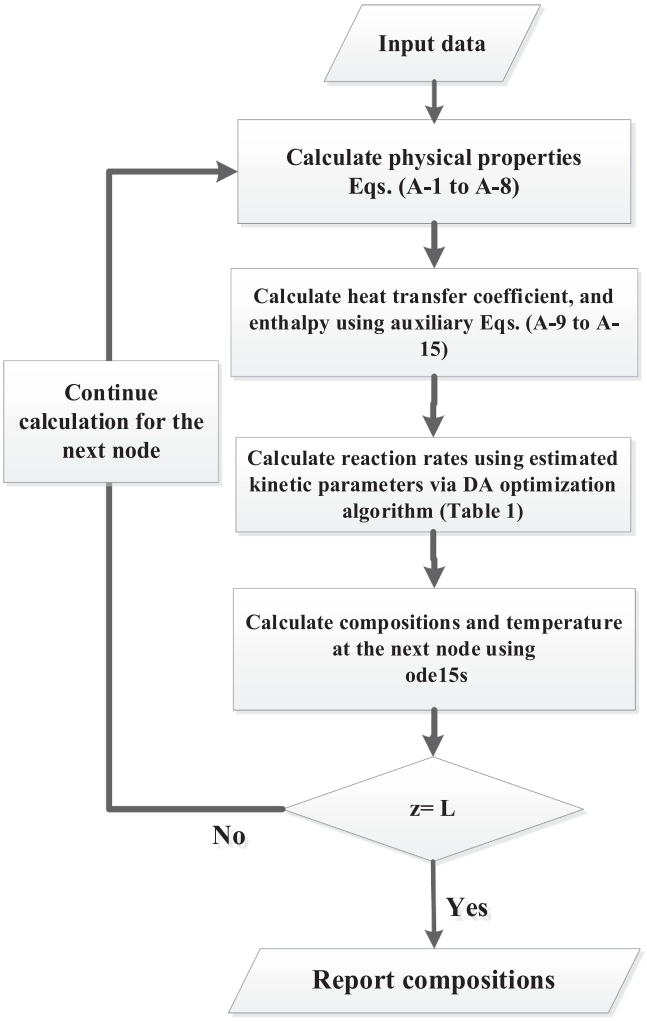

Fig. 4. Algorithm for solving the proposed model.

implementation of SI-based algorithms in scientific and industrial optimization problems is an indication of their merits in practice namely: 1) in contrast to evolutionary algorithms (EA), in the DA method and other SI-based techniques, the information about the search space are saved during the optimization. 2) Fewer controlling parameters are used in this method. 3) Less operators are used in this method. 4) The flexibility of this method makes it applicable in various fields. The main inspiration of the DA originates from static and dynamic swarming behaviors. In fact, static and dynamic swarms are comparable to the two meta-heuristic phases of optimization, i.e. exploration and exploitation. In other words, small sub-swarms of dragonflies fly in short and different distances in a static swarm as the principle goal of the exploration. However, sizable populations of dragonflies fly all in one sizable direction, which is the main aim of exploitation. The mathematical implementation of these two phases are presented in Appendix B [52].

The optimization process by DA is started by producing several random sets of solutions. Indeed, random values are used to initialize the position and step vectors between the lower and upper bounds of the variables. During every iteration, Eq. (B-6), Eq. (B-7) and Eq. (B-8) are used to update the position and step for each dragonfly. The neighborhood of every dragonfly is selected via the calculation of Euclidean distance among all dragonflies and choosing N of them updating the vectors of X and ΔX. This updating of the position is iteratively continued while the criterion satisfied [52]. Therefore, the kinetic parameters can be estimated via minimization of the objective function,

Table 2
Estimated kinetic data via DA optimization algorithm.

Reactions	k (mol/(s.g.MPa))		a_{i,H_2O}	b_{i,CO_2}	E(kJ/mol)
CO_2 Shift	61,164,952	$B_1 = 2250$ $B_2 = 2.45$	61.48	5.5	131.67
FT (CH_4)	24,267,501		42.05	2.42	126.54
FT (C_2H_4)	32,018,339		42.18	2.31	123.12
FT (C_2H_6)	24,110,786		45.93	2.52	131.67
FT (C_3H_6)	33,151,357		41.95	2.25	117.99
FT (C_3H_8)	24,620,154		45.56	2.55	128.25
FT (C_4H_8)	2,329,745		45.92	3.34	119.7
FT (C_4H_{10})	335,740		46.11	3.74	119.7

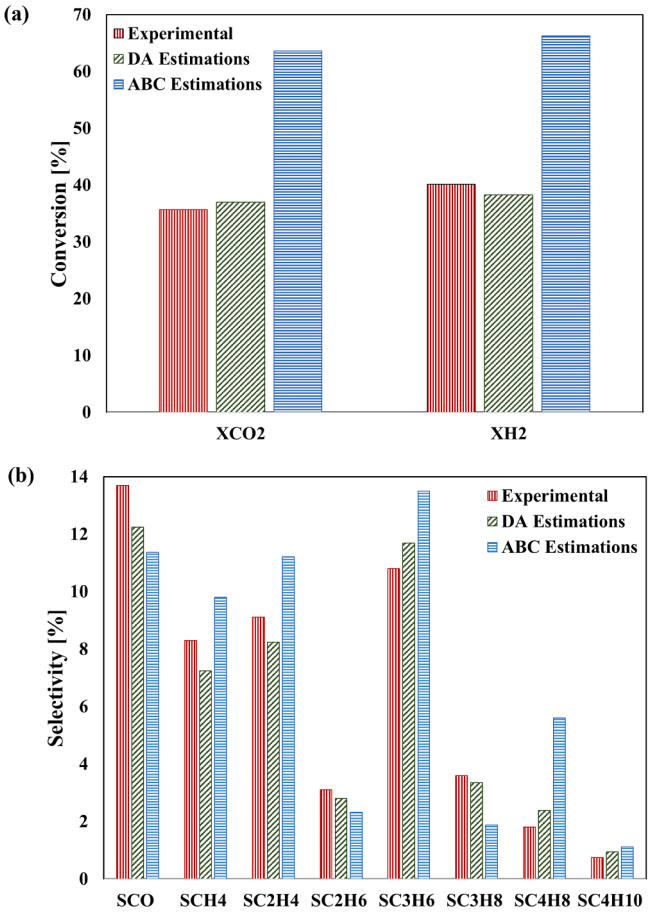

Fig. 5. Comparison of the experimental data in terms of a) conversions and b) products selectivity in CR using DA and ABC optimization algorithms.

which is the root mean square error (RMSE), (minimizing the difference between modeling predictions and experimental data) as represented in Eq. (26). The DA flowchart is demonstrated in Fig. 3.

$$O.F = Min\left(\sqrt{\frac{\sum_{i=1}^{N}\left(Y_{exp,i} - Y_{model,i}\right)^2}{N}}\right) \quad (26)$$

4. Results and discussion

The proposed models have been solved by *ode15s* codes in MATLAB according to the algorithm presented in Fig. 4, and the performances of AFSR, RFSR and CR are compared to achieve a more comprehensive

Table 3
Comparison of available experimental data with estimated values using DA and ABC optimization algorithms.

Parameters	Exp. data	Kim et al. [58]	Kim et al. [59]	Lee et al. [55]	DA Estimations	ABC Estimations
XCO_2	35.7	35.6	32.3	40.8	37.001	63.583
XH_2	40.1	–	–	–	38.297	66.297
S_{CO}	13.7	9.6	11	11.1	12.242	11.366
SCH_4	8.3	10.9	8.5	7.4	7.239	9.811
SC_2H_4	9.11	5.8	5.1	5.8	8.244	11.213
SC_2H_6	3.1	3.2	1.9	1.4	2.800	2.321
SC_3H_6	10.8	11.6	9.4	9.6	11.691	13.505
SC_3H_8	3.6	2.9	3.4	1.1	3.346	1.876
SC_4H_8	1.8	9.3	8	7	2.391	5.599
SC_4H_{10}	0.75	2.4	3.6	0.9	0.940	1.117

understanding of the influence of the reactor configuration on the CO_2 hydrogenation process.

4.1. Estimation of kinetic parameters

The kinetic parameters of the rate expressions in Table 1 are estimated via fitting the experimental and modeling data through DA optimization algorithm and presented in Table 2. The experimental data were obtained in a SS316 reactor with 60 cm length while inside and outside diameters were 0.8 and 1.2 cm, respectively. Typically, in the designed experiments for kinetics parameter derivation, 1.5 to 5 gr of K-Fe/Al_2O_3 catalyst diluted with glass beads was used [50].

In addition, the ABC algorithm is also used to predict the kinetic parameters, and the comparison of the estimations are presented in Fig. 5. To assess the precision of these algorithms, the estimated results are compared to the available experimental data in terms of reactant conversions and products distribution in Table 3. The products distribution are in accordance with the previously reported trends in literature [53–57]. According to Fig. 5 (a), it can be observed that ABC algorithm overestimates the conversions, like the predictions in the previous paper [50], while DA could provide more reliable estimations (about 4% error compared to experimental data). The ability to search the feature space adaptively while avoiding premature convergence is one of the main advantages of DA algorithm. Moreover, this algorithm is capable of balancing between exploration and exploitation while exhibiting a good ability to converge the global optimum instead of falling in local minima.

The performance of CR reactor in terms of products yield and temperature profile by using the estimated kinetic parameters are illustrated in Fig. 6. According to Fig. 6 (a), it can be observed that CO first produced via RWGS reaction and then consumes through FT reactions, which results in the occurrence of a maximum point in the plot. The hydrocarbons are gradually produced via CO consumption (FT reaction) and the products distribution are as follows: $C_3H_6 > C_2H_4 > CH_4 > C_3H_8 > C_2H_6 > C_4H_8 > C_4H_{10}$. Initially, the temperature decreases a bit due to the occurrence of the endothermic RWGS reaction, as shown in Fig. 6 (b), while the exothermic nature of FT reactions increases the temperature. However, the constant jacket temperature (at 300 °C) prohibits further temperature increase, and thus can avoid hot spot formation. Finally, the reactor temperature reduces and approaches to the jacket temperature (300 °C).

4.2. Comparing the performance of cylindrical and spherical reactors

Spherical reactors have been considered as a promising candidate for pilot/industrial reactors due to their cost-effectiveness and flexibility in operating conditions [60,61]. To compare the performance of CR, AFSR and RFSRs in CO_2 hydrogenation to hydrocarbons, spherical reactors are assumed to have 1) the same volume and 2) the same surface area with that of CR.

4.2.1. The performance of an axial flow spherical reactor (AFSR)

The performance of AFSR-1 (with the same volume to that of CR) and AFSR-2 (with the same surface area to that of CR) in CO_2 hydrogenation to hydrocarbons are compared, and the results are displayed in Fig. 7.

It can be observed that, the performance of AFSR-2 is higher in terms of both conversion and hydrocarbons selectivity with respect to both CR and AFSR-1, while there is no considerable difference between the performances of CR and AFSR-1. Therefore, the AFSR can be effective only when the surface area (not the volume) of the spherical reactor is the same as that of CR, which can be an indication of the role of heat transfer surface area for this system. The heat transfer surface area of the

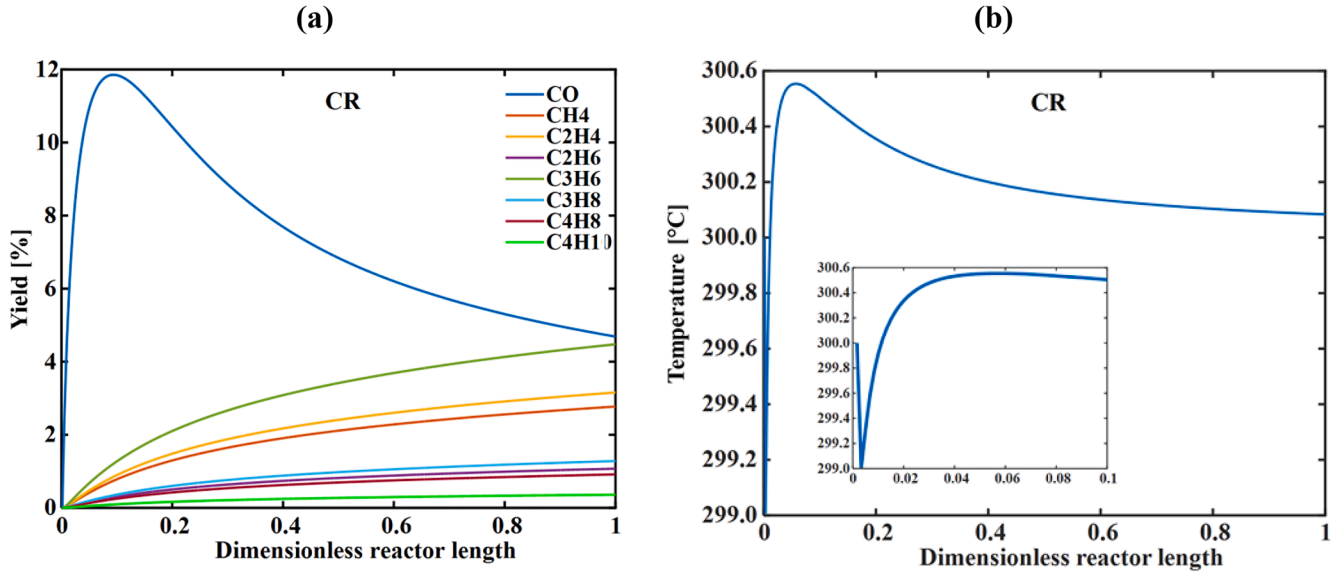

Fig 6. a) Yield of products and b) Temperature profile in the CR at $T_0 = 300$ °C, $P_0 = 1$ MPa and SV = 2 L/g_{cat}. h.

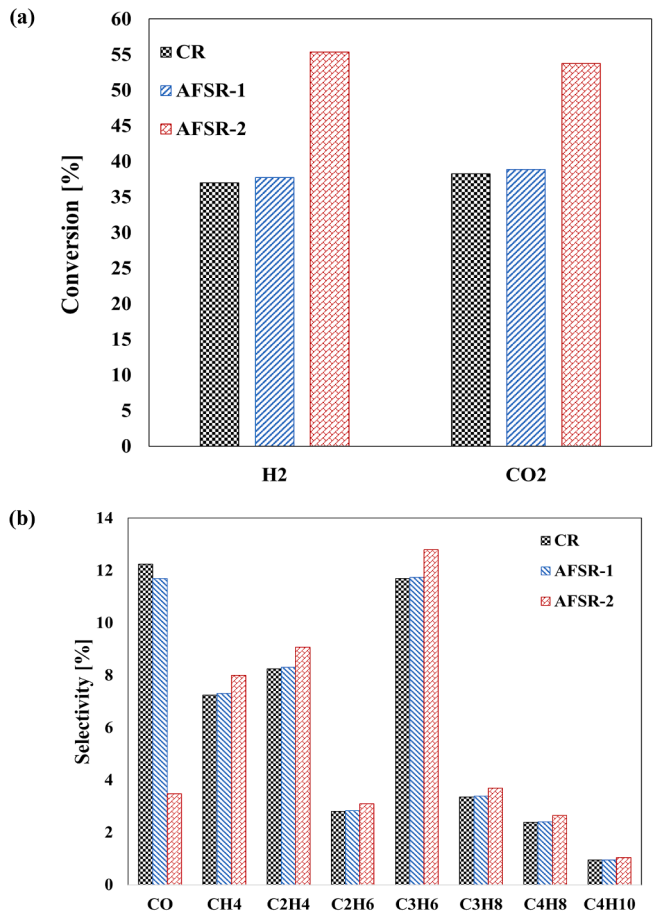

Fig. 7. a) Reactant conversions and b) products distribution in CR, AFSR-1 and AFSR-1 at $T_0 = 300$ °C, $P_0 = 1$ MPa and SV = 2 L/g_{cat}. h.

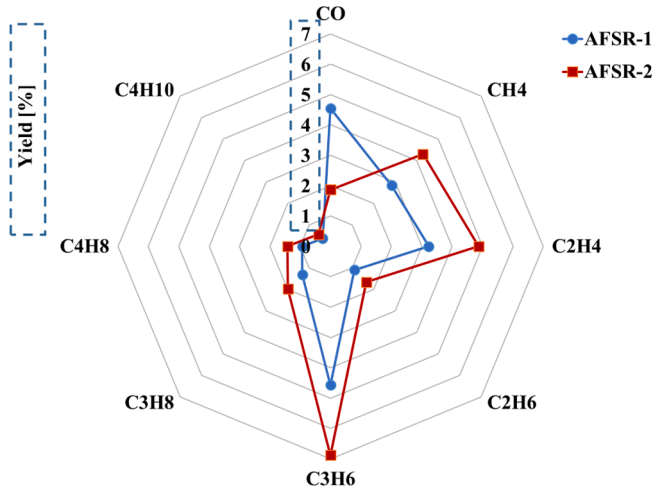

Fig. 8. Comparing the products yield in the AFSR-1 and AFSR-2 at $T_0 = 300$ °C, $P_0 = 1$ MPa and SV = 2 L/g_{cat}. h.

reactor is the outer surface of the reactor (reactor wall), which is in contact with the jacket. Therefore, a large surface area can provide higher heat transfer rate. Since the surface area of AFSR-2 is larger than that of AFSR-1, the required heat of RWGS reaction can be provided easier, which led to higher CO_2 conversion and in turn, production of more CO, which is the feed for FT reaction. The higher conversions in AFSR-2 results in higher hydrocarbons yield in AFSR-2, as shown in

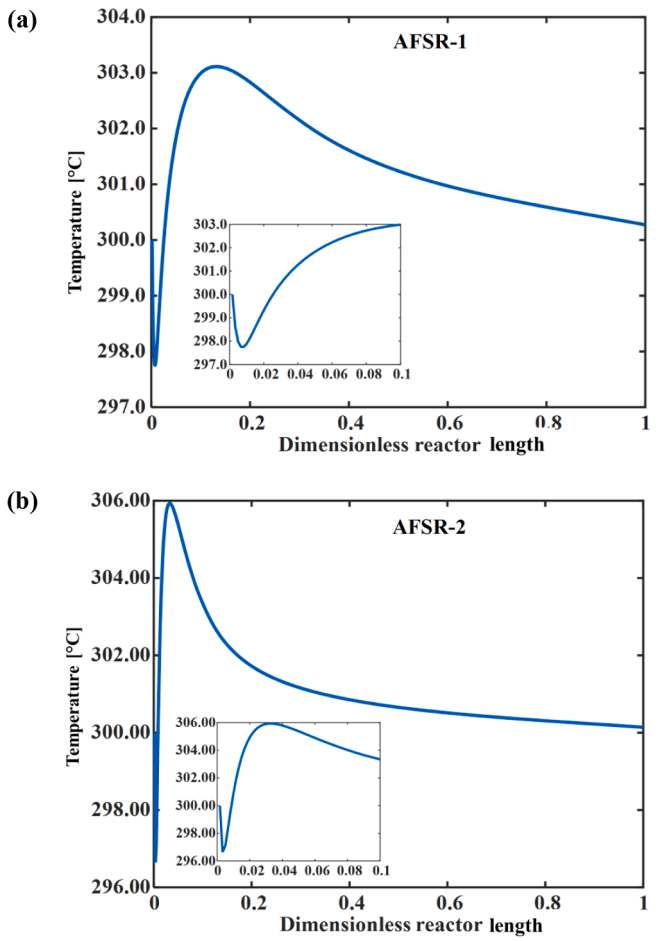

Fig. 9. Temperature profile in the a) AFSR-1 and b) AFSR-2 at $T_0 = 300$ °C, $P_0 = 1$ MPa and Vs = 2 L/g_{cat}. h.

Fig. 8.

In Fig. 8, it can be observed that CO yield is lower in AFSR-2, which shows that the production and consumption of CO occur faster in AFSR-2, which may be attributed to its larger volume. This results in the production of more hydrocarbons (especially CH_4 and light olefins (C_2H_4 and C_3H_6)). As a whole, compared to CR, the total yield of hydrocarbons in AFSR-2 increased by about 54.5%, while in AFSR-1 only 2.3% increase is achieved.

According to Fig. 9, it can be observed that the trends of temperature changes are the same in both reactors, and also similar to that of CR, while the extents of temperature fluctuations differ. It can be observed that, the performance of CR and AFSR-1 (Fig. 7) are approximately similar since their volumes are assumed the same, while the temperature profiles of the corresponding reactors are different according to Fig. 6 (b) and Fig. 9 (a). In order to analyze these temperature differences in various reactors, two main terms of the energy balance equations (Eq. (14), Eq. (17) and Eq. (22)), are separately calculated via Eq. (27) to Eq. (30) and illustrated in Fig. 10.

$$\text{The heat of reaction} = \sum_{j=1}^{9} \rho_p (1-\varepsilon_b) r_j \left(-\Delta H_{f,j}\right) \tag{27}$$

$$\text{Heat transfer by the jacket in CR} = \frac{4U_c}{D_c} T_j \tag{28}$$

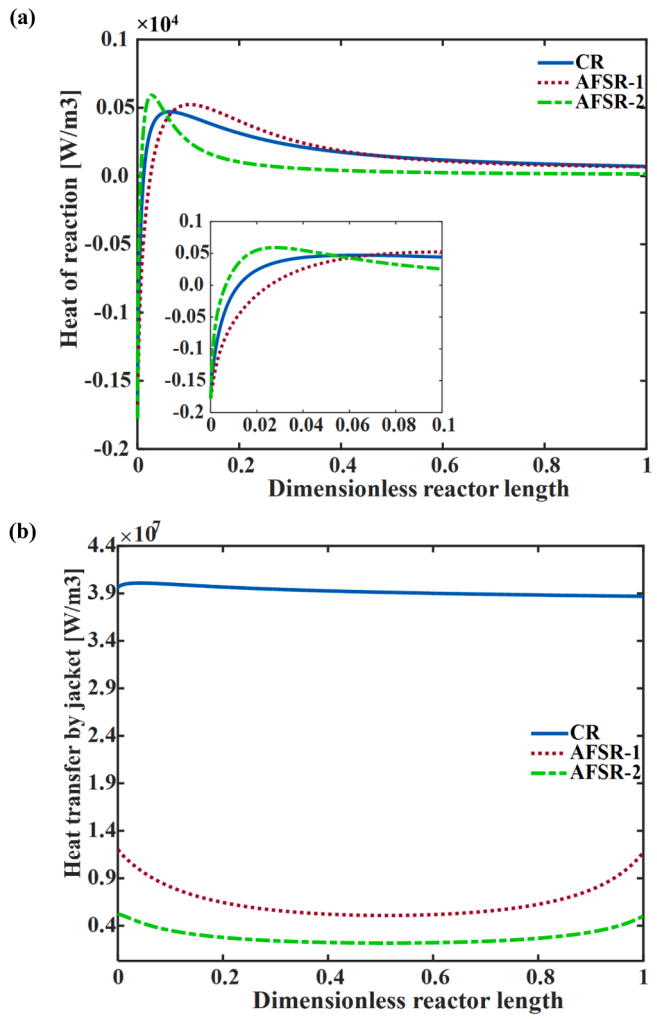

Fig. 10. Comparison of a) reaction heat and b) heat transfer by jacket in AFSRs and CR at $T_0 = 300$ °C, $P_0 = 1$ MPa and SV = 2 L/g_{cat}. h.

$$\text{Heat transfer by the jacket in AFSR} = \frac{2\pi r_z U_z}{A_z} T_j \tag{29}$$

$$\text{Heat transfer by the jacket in RFSR} = \frac{8\pi r U_r}{A_r} T_j \tag{30}$$

Since the net balances of the heat of reaction are approximately the same in these reactors (Fig. 10 (a)), the temperature difference can be attributed to the larger and varying diameter of the AFSR-1 compared to that of CR, which reduces the controlling role of jacket temperature as can be observed in Fig. 10 (b). Simultaneous occurrence of the endothermic RWGS and exothermic FT reactions in the reactor leads to the question of suitable reaction temperatures. Under kinetic control regime, both RWGS and FT reaction kinetically increase with increasing temperatures (the energy barriers can be overcome more easily). However, the conversion to hydrocarbons requires lower temperatures to shift the reaction equilibria towards hydrocarbons. Coupled exothermic/endothermic reactions have been discussed in the literature [62,63]. Therefore, the net heat of reaction is initially negative in Fig. 10 (a), which is an indication of positive enthalpy according to Eq. (27); gradually, the reaction heat becomes positive after a while (negative enthalpy), which shows the progress of FT reactions. However,

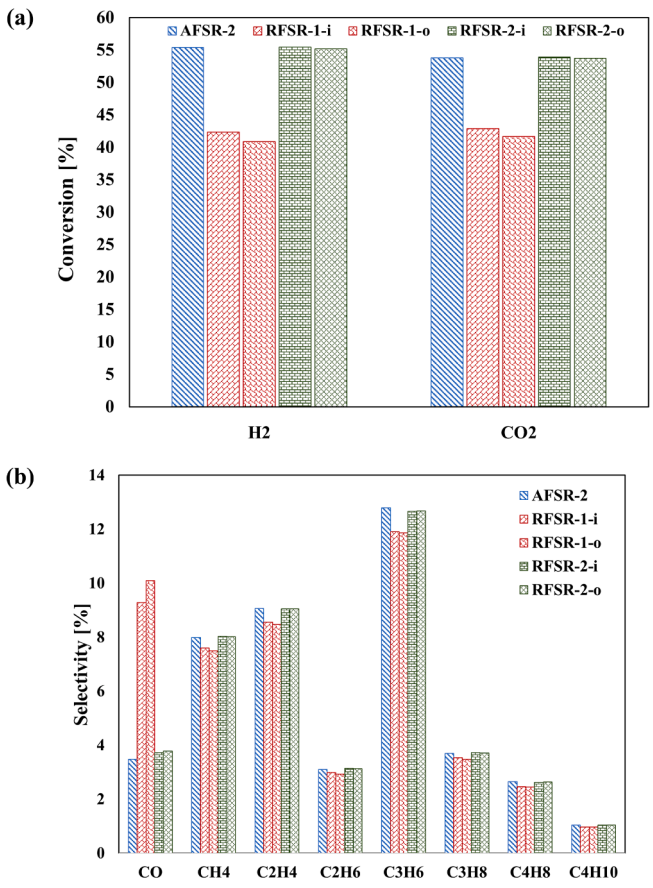

Fig. 11. a) Reactant conversions and b) products distribution in CR, RFSR-1-i and RFSR-1-o at $T_0 = 300$ °C, $P_0 = 1$ MPa and SV = 2 L/g_{cat}. h.

the constant jacket temperature (300 °C) inhibits further temperature increase to avoid hot spot and causes the reactor temperature to eventually reach the jacket temperature.

In AFSR-2, the lateral surface area assumed the same with that of CR, which results in a larger diameter and volume for the reaction. Therefore, higher performance is achieved as observed in Fig. 7 and the net heat of reaction would be higher (Fig. 10 (a)). In addition, since the jacket temperature is the same in both AFSRs, the temperature augmentation would be higher in AFSR-2 (since the heat ofFT reaction could not be released) as can be observed in Fig. 10 (b). The radial flow spherical reactors are also analyzed in the following section to assess the role of flow pattern on the performance of spherical reactors.

4.2.2. *The performance of radial flow spherical reactor (RFSR)*

The performance of RFSR-1 (with the same volume of CR) and RFSR-2 (with the same surface area of CR) presented in Fig. 11 in terms of reactants conversion and products selectivity, and compared with the performance of the best reactor in the previous section, AFSR-2. Each reactor has two possibilities for jacket location: inside and outside, which are shown with i and o.

It can be observed that, RFSR-2 (both i and o) have better performance compared to RFSR-1. Moreover, the performance of RFSR-2-i is almost the same as that of AFSR-2. Therefore, it can be deduced that, when the surface areas of the spherical reactors are considered the same as the lateral area of the CR, better results can be achieved compared to the reactors with the same volumes. In addition, when the jacket is

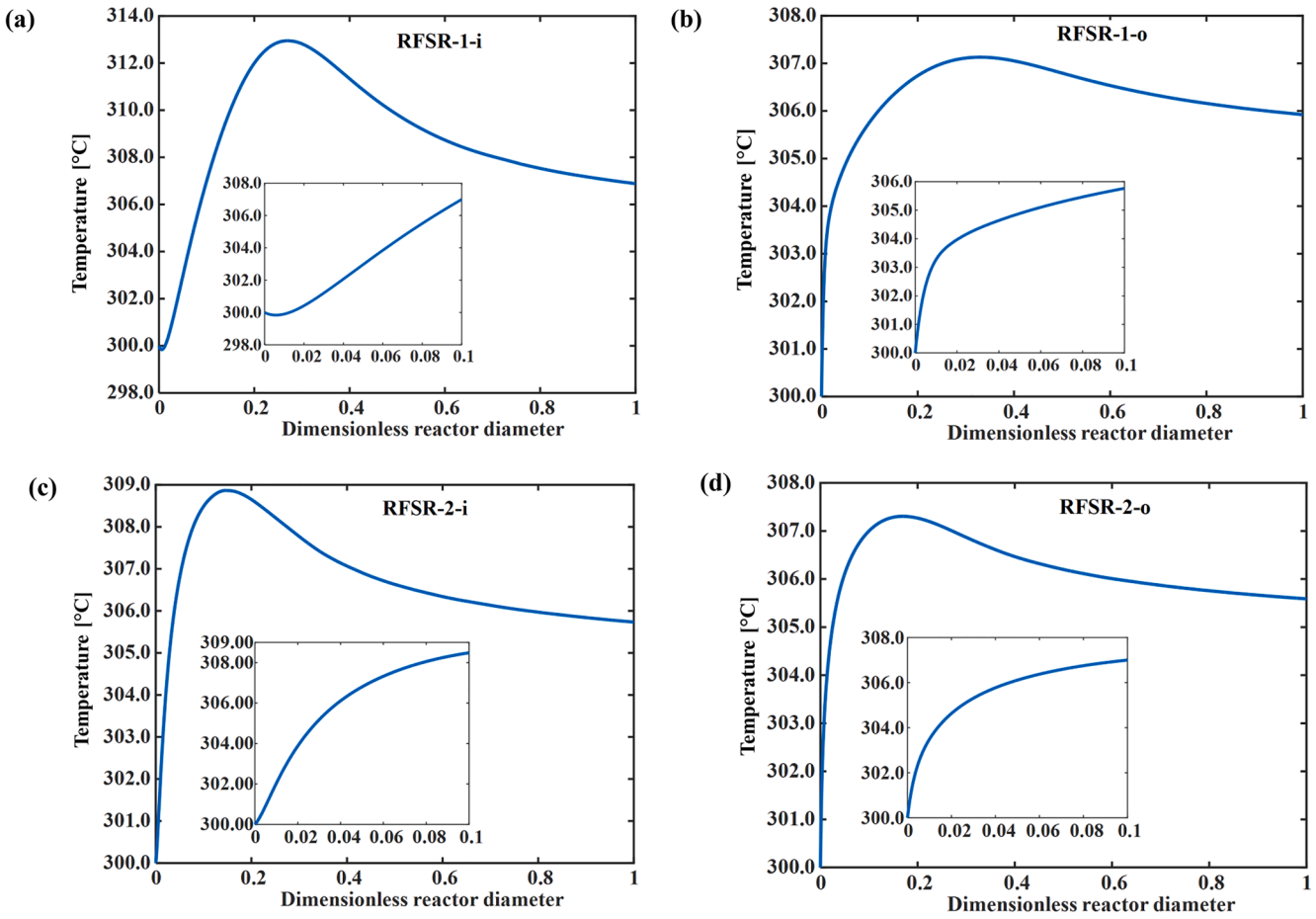

Fig. 12. Temperature profiles in the a) RFSR-1-i, b) RFSR-1-o, c) RFSR-2-i and d) RFSR-2-o at $T_0 = 300$ °C, $P_0 = 1$ MPa and SV = 2 L/g_{cat}. h.

located inside the spherical reactor, the performance seems to be better. However, the temperature profiles are not the same and illustrated separately in Fig. 12. As mentioned previously, the jacket is located inside in the RFSR-1-i and RFSR-2-i and outside in RFSR-1-o and RFSR-2-o.

In RFSRs it can be observed that, RFSR-1-i (Fig. 12 (a)) and RFSR-2-i (Fig. 12 (c)) with inner jackets undergo larger temperature changes compared to those of RFSR-1-o (Fig. 12 (b)) and RFSR-2-o (Fig. 12 (d)) with outer jackets. Therefore, in the radial configuration, the influence of jacket position is more important than the reactor diameter.

Fig. 13 illustrates the impacts of reaction heat and jacket location on the reactor temperature and explaining the differences in temperature profiles, as observed in Fig. 12. As can be observed in Fig. 13 (a), the heats of reaction are approximately in the same range. However, the graphs are wider in RFSRs with respect to that of AFSR-2, which shows that in AFSR-2, reactions occur faster. Indeed, as the reactor volume decreases, the graphs become wider and vice versa. Moreover, according to Fig. 13 (b), the heat transfer by jacket is larger in the order of RFSR-1-o RFSR-2-o RFSR-2-i RFSR-1-i, which shows that the role of jacket position is more important than that of reactor volume. In fact, when the jacket is located on the outer surface, the reactor temperature can be controlled better regardless of its volume. Besides, the heat transfer by the jacket in AFSR-2 is smaller than those of RFSRs until L = 0.5, while it increases and becomes the largest at the end of the reactor.

As a whole, comparing CR, AFSRs and RFSRs demonstrates that the highest CO_2 conversions belong to RFSR-2-i and AFSR-2 (X_{CO2} = 53.891%, X_{CO2} = 53.763%), while the selectivity towards hydrocarbons in these reactors are 40.286% and 40.330% as can be observed in Table 4.

Indeed, the reaction occurs faster in AFSR-2 with respect to RFSR-2-i (Fig. 13 (a)), while the net heat of reaction is approximately the same (the maximum point in Fig. 13 (a)). It is noteworthy that, both of these two reactors have the same lateral surface area with that of CR, which results in larger volumes than that of CR. The AFSR-2 exhibited the largest surface area and volume among other reactors. In addition, the temperature increase in AFSR-2 is less than that of RFSRs, which is an indication of better temperature control in the axial mode rather than radial for this system. In the case of similar volumes, AFSR-1 cannot provide a better performance, while RFSR-1-i and RFSR-1-o are able to increase CO_2 hydrogenation performance with respect to CR and not AFSR-2.

The pressure drop in all reactors are illustrated in Fig. 14, and it can

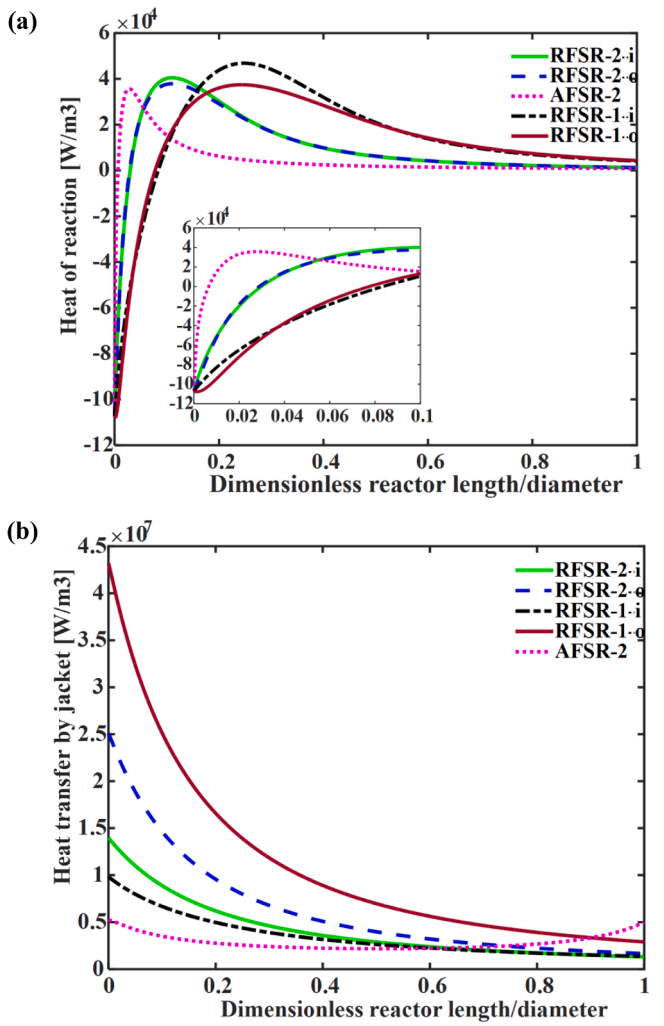

Fig. 13. Comparison of a) reaction heat and b) heat transfer by jacket in RFSRs and AFSR-2 at T_0 = 300 °C, P_0 = 1 MPa and SV = 2 L/g_{cat}. h.

be observed that at the same operating conditions the spherical reactors provide considerable lower pressure drop compared to that of CR [64]. It can be attributed to the changes in cross sectional area, which results in lower velocity and in turn, decreased pressure drop.

As a whole, mathematical modeling is a fast and effective tool to study, analyze and estimate the performance of reactors in various conditions without too many experiments, while provides a comprehensive understanding of important factors. However, innovative techniques are yet required to enhance the efficiency of CO_2 hydrogenation process, while reducing volumes and costs [65,66].

5. Conclusions

Exploiting DA optimization algorithm, kinetic parameters of CO_2 hydrogenations were estimated using the proposed pseudo-homogeneous one-dimensional non-isothermal model. It was revealed that, in contrast to the ABC algorithm, DA algorithm could predict the conversion of the reactants with less than 4% error compared to experimental data. In addition, the modeling results of CR were in great accordance with the available literature data. The proposed model was used to compare the influence of reactor configuration on the CO_2 hydrogenation to hydrocarbons employing the estimated kinetic parameters. Both axial and radial flow spherical reactors were investigated with 1- the same volume and 2- the same surface area with those of CR. In addition, in RFSRs, two possibilities for jacket location i.e. i- inside and o- outside, were considered. Comparing with CR, it was inferred that spherical reactors could provide better CO_2 hydrogenation performance. It was concluded that, AFSR-2 and RFSR-2-i could provide the highest performance in terms of CO_2 conversion (X_{CO2} = 53.763%, X_{CO2} = 53.891%) and hydrocarbons selectivity (S_{HC} = 40.330%, S_{HC} = 40.286%). Moreover, the temperature increase in these reactors were less than those observed in RFSRs. In RFSRs, temperature fluctuations were better controlled via constant-temperature jacket in RFSR-1-o and RFSR-2-o, which was attributed to the importance of jacket location (outer surface) regardless of reactor volume. In addition, results revealed that spherical reactors provided considerably lower pressure drop compared to that of CR.

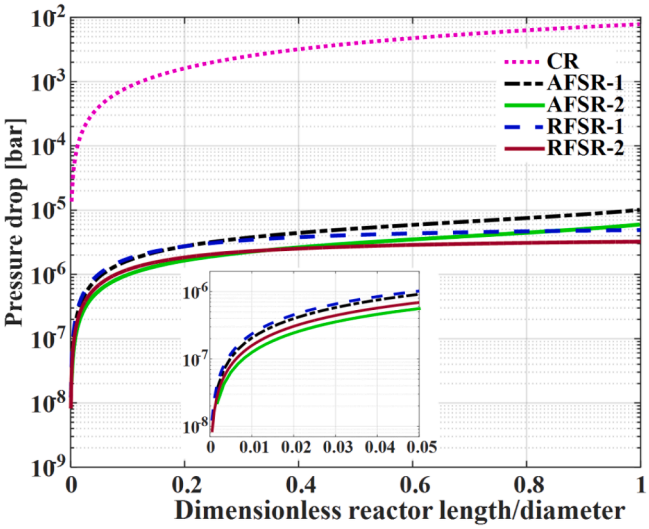

Fig. 14. Pressure profile in different reactors at T_0 = 300 °C, P_0 = 1 MPa and SV = 2 L/g_{cat}. h.

Table 4
Performance of modeled reactors in CO_2 hydrogenation to hydrocarbons.

	CR	AFSR-1	AFSR-2	RFSR-1-i	RFSR-1-o	RFSR-2-i	RFSR-2-o
XH_2	37.001	37.748	55.359	42.358	40.89	**55.412**	55.183
XCO_2	38.297	38.899	53.763	42.856	41.631	**53.891**	53.687
S_{CO}	12.242	11.688	3.471	9.2845	10.099	3.7305	3.7825
SCH_4	7.2391	7.3049	7.992	7.5998	7.4922	8.0308	8.0175
SC_2H_4	8.2442	8.3018	9.0627	8.549	8.4631	9.0545	9.0479
SC_2H_6	2.8001	2.8337	3.0993	2.9901	2.9305	3.1411	3.1317
SC_3H_6	11.691	11.737	12.79	11.909	11.861	12.669	12.677
SC_3H_8	3.3456	3.3791	3.695	3.5317	3.475	3.7236	3.7158
SC_4H_8	2.3914	2.4048	2.646	2.4597	2.4424	2.629	2.6292
SC_4H_{10}	0.94021	0.94577	1.0446	0.96863	0.96137	1.038	1.038
S_{HC}	36.652	36.907	**40.330**	38.008	37.625	40.286	40.257

CRediT authorship contribution statement

Sara Najari: Writing - original draft. **Samrand Saeidi:** Conceptualization, Methodology, Writing - review & editing, Data curation. **Gyula Grófi:** Investigation, Writing - review & editing. **Frerich J. Keil:** Writing - review & editing, Supervision. **Alirio E. Rodrigues:** Supervision.

Declaration of Competing Interest

The authors declare that they have no known competing financial interests or personal relationships that could have appeared to influence the work reported in this paper.

Acknowledgments

The research reported in this paper and carried out at BME has been supported by the NRDI Fund (TKP2020 NC, Grant No. BME-NCS) based on the charter of bolster issued by the NRDI Office under the auspices of the Ministry for Innovation and Technology.

Appendix A. Required correlations

Physical properties [19]

$$\rho_g = \frac{MwP}{RT} \tag{A-1}$$

$$\rho_B = (1-\varepsilon_b)\rho_p \tag{A-2}$$

Heat capacity [67]

$$C_{pg} = \sum_{i=1}^{Ns} y_i C_{pg,i};$$
$$\frac{C_{pg,i}}{R} = A0_i + A1_i \times T + A2_i \times T^2 + A3_i \times T^3 + A4_i \times T^4 \tag{A-3}$$

Thermal conductivity [68]

$$K_g = \sum_{i=1}^{N} \frac{y_i K_{g,i}}{\sum_{j=1}^{N} y_j \theta_{ij}};$$
$$K_{g,i} = \frac{B1_i T^{B2_i}}{1 + \frac{B3_i}{T} + \frac{B4_i}{T^2}} \tag{A-4}$$

$$\theta_{ij} = \frac{1}{4} \times \left[1 + \left[\left(\frac{\mu_i}{\mu_j}\right)\left(\frac{Mw_j}{Mw_i}\right)^{\frac{3}{4}}\left(\frac{T+S_i}{T+S_j}\right)\right]^{\frac{1}{2}}\right]^2 \times \frac{(T+S_{ij})}{(T+S_i)};$$
$$S_{ij} = f_s\sqrt{S_i S_j} \tag{A-5}$$

$$f_s = \begin{cases} 1 & nonpolar \\ 0.733 & polar \end{cases}$$
$$S_{i\ or\ j} = \begin{cases} 79 & for\ H_2\ only \\ 1.5 \times T_{B,i} & for\ other\ components \end{cases} \tag{A-6}$$

Viscosity [68]

$$\mu_g = \sum_{i=1}^{N} \frac{y_i \mu_{g,i}}{\sum_{j=1}^{N} y_j \phi_{ij}};$$
$$\mu_{g,i} = \frac{C1_i T^{C2_i}}{1 + C3_i + \frac{C4_i}{T^2}} \tag{A-7}$$

$$\phi_{ij} = \frac{\left[1 + \left(\frac{\mu_{g,i}}{\mu_{g,j}}\right)^{1/2}\left(\frac{Mw_j}{Mw_i}\right)^{1/4}\right]^2}{\left[8\left(1 + \frac{Mw_i}{Mw_j}\right)\right]^{1/2}} \tag{A-8}$$

Auxiliary equations

Heat transfer coefficient [69]

$$h_r = 0.4\frac{K_g}{D_p}\left(2.58Re^{1/3}Pr^{1/3} + 0.094Re^{0.8}Pr^{0.4}\right) \tag{A-9}$$

Table A1
Constants for gas species corresponding to Eq. (A-3) [67].

Components	A0	A1 × 10^{-3}	A2 × 10^{-5}	A3 × 10^{-8}	A4 × 10^{-11}	ΔH_T^0(kJmol^{-1})
H_2	2.883	3.681	−0.772	0.692	−0.213	0
CO_2	3.259	1.356	1.502	−2.374	1.056	−393.51
CO	3.912	−3.913	1.182	−1.302	0.515	−110.53
CH_4	4.568	−8.913	3.631	−3.407	1.091	−74.52
C_2H_4	4.221	−8.782	5.795	−6.729	2.511	52.5
C_2H_6	4.178	−4.427	5.660	−6.651	2.487	−83.82
C_3H_6	3.834	3.893	4.688	−6.013	2.283	20
C_3H_8	3.847	5.131	6.011	−7.893	3.079	−104.68
C_4H_8	4.389	7.984	6.143	−8.197	3.165	−0.54
C_4H_{10}	5.547	5.536	8.057	−10.571	4.134	−125.79
H_2O	4.395	−4.186	1.405	0.157	0.632	−241.81

Table A2
Constants for gas species corresponding to Eq. (A-4) [68].

Components	B1	B2	B3	B4	T_B (K)
H_2	2.653 × 10^{-3}	0.7452	12	0	20.4
CO_2	3.69	−0.3838	964	1.86 × 10^6	194.7
CO	5.988 × 10^{-4}	0.6863	57.13	501.92	81.7
CH_4	8.398 × 10^{-6}	1.4268	−49.654	0	111.7
C_2H_4	8.681 × 10^{-6}	1.4559	299.72	−2.940 × 10^4	169.4
C_2H_6	7.387 × 10^{-5}	1.1689	500.73	0	184.5
C_3H_6	4.49 × 10^{-5}	1.2018	421	0	225.4
C_3H_8	−1.12	0.10972	−9834.6	−7.536 × 10^6	231.1
C_4H_8	9.681 × 10^{-5}	1.1153	781.82	0	266.9
C_4H_{10}	5.109 × 10^{-2}	0.45253	5455.5	1.98 × 10^6	272.7
H_2O	6.204 × 10^{-6}	1.3973	1.3973	0	373.2

$$U_C = \left(\frac{1}{h_r} + A_{l,c} \frac{\ln \frac{R_i}{R_o}}{2\pi K_w L} \right)^{-1} \tag{A-10}$$

$$U_z = \left(\frac{1}{h_r} + A_{l,ax}(z) \frac{\ln \frac{R_j(z)}{R_o(z)}}{2\pi K_w} \right)^{-1} \tag{A-11}$$

$$U_r = \left(\frac{1}{h_r} + A_{l,rdl,i} \frac{R_i - R_j}{4\pi R_i R_j K_w} \right)^{-1} \quad \left(Inside\ jacket \right); \qquad U_r = \left(\frac{1}{h_r} + A_{l,rdl,o} \frac{R_j - R_o}{4\pi R_j R_o K_w} \right)^{-1} \quad \left(Outside\ jacket \right) \tag{A-12}$$

$$Re = \frac{\rho_g u_g D_p}{\mu_g} \tag{A-13}$$

$$Pr = \frac{C_{pg} \mu_g}{K_g} \tag{A-14}$$

$$u_g = \frac{V_s}{A_c \varepsilon_b}; \qquad V_s = m_{cat} V_{s0} \times \frac{T}{273.15} \times \frac{101325}{P} \tag{A-15}$$

Enthalpy of reaction

$$\Delta H_T = \Delta H_T^0 + \int_{T_0}^{T} \Delta C_p dT \tag{A-16}$$

$$\Delta H_T = \Delta H_T^0 + R\left(\Delta A_0 T + \Delta A_1 \frac{T^2}{2} + \Delta A_2 \frac{T^3}{3} + \Delta A_3 \frac{T^4}{4} + \Delta A_4 \frac{T^5}{5} \right) - I \tag{A-17}$$

$$I = R\left(\Delta A_0 T_0 + \Delta A_1 \frac{{T_0}^2}{2} + \Delta A_2 \frac{{T_0}^3}{3} + \Delta A_3 \frac{{T_0}^4}{4} + \Delta A_4 \frac{{T_0}^5}{5} \right) \tag{A-18}$$

$$\Delta A_i = \sum \nu_k A_{i,k} \tag{A-19}$$

Appendix B. Dragonfly algorithm

Three main parts of the swarm's behavior are separation, alignment and cohesion. The first one means avoiding the static collision between dragonflies. The second shows the relative velocity of dragonflies, and the third is an indication of the tendency of each dragonfly to the center of the population of dragonflies in the neighborhood. Survival is the main goal of each swarm; therefore, each dragonfly should turn away from enemies while approaching to food. Accordingly, five parameters are used to update the position of each dragonfly. These behaviors can be modeled as follows [52]:

Table A3
Constants for gas species corresponding to Eq. (A-7) [67].

Components	C1	C2	C3	C4
H_2	1.79×10^{-7}	0.685	−0.59	140
CO	1.1127×10^{-6}	0.5338	94.7	0
CO_2	2.148×10^{-6}	0.46	290	0
CH_4	5.2546×10^{-7}	0.59006	105.67	0
C_2H_4	2.0789×10^{-6}	0.4163	352.7	0
C_2H_6	2.5906×10^{-7}	0.67988	98.902	0
C_3H_6	7.73919×10^{-7}	0.5423	263.73	0
C_3H_8	$4.9054e \times 10^{-8}$	0.90125	0	0
C_4H_8	6.9744×10^{-7}	0.5462	305.25	0
C_4H_{10}	3.4387×10^{-8}	0.94604	0	0
H_2O	1.7096×10^{-8}	1.1146	0	0

Separation, alignment and cohesion can be defined according to **Eq. (B-1)**, **Eq. (B-2)**, and **Eq. (B-3)**.

$$S_i = -\sum_{j=1}^{N} X - X_j \tag{B-1}$$

$$A_i = \frac{\sum_{j=1}^{N} V_j}{N} \tag{B-2}$$

$$C_i = \frac{\sum_{j=1}^{N} X_j}{N} - X \tag{B-3}$$

where N is the number of neighboring dragonflies, X is the position of one distinct dragonfly, X_j is the position of j-th dragonfly in the neighborhood, V_j is the velocity of the j-th dragonfly.

Attraction to the food and distraction from enemies can be written as **Eq. (B-4)** and **Eq. (B-5)**:

$$F_i = X^+ - X \tag{B-4}$$

$$E_i = X^- - X \tag{B-5}$$

where X^+ and X^- are the positions of food and enemy. These five parameters are assumed to show the behavior of dragonflies. To update the positions of dragonflies and simulating their behavior, ΔX is defined as step vector, which shows the movement directions and can be defined as follows:

$$\Delta X_{t+1} = (sS_i + aA_i + cC_i + fF_i + eE_i) + w\Delta X_t \tag{B-6}$$

$$X_{t+1} = X_t + \Delta X_{t+1} \tag{B-7}$$

Where s, a, c, f and e are separation weight, alignment weight, cohesion weight, food factor and enemy factor, respectively. While, w and t are inertia weight and iteration counter, respectively., Various exploration and exploitation behaviors can be achieved during the optimization process using these parameters. Since the neighbors of the dragonflies are very significant, a neighborhood with a definite radius is considered.

As described previously, dragonflies have static and dynamic swarms. In a dynamic swarm, they try to align with appropriate separation and cohesion, while in static swarms they fly with low alignment and high cohesion to the preys. Consequently, in the exploring phase, the dragonflies are assigned with high alignment and low cohesion weights in contrast to those of the exploitation phase. Increasing the radii of neighborhoods proportional to the iteration number results in transition between these two phases. Another method is to tune the weights during the optimization process to balance these phases.

The convergence can be guaranteed by adaptively changing the weights for the transition between exploration and exploitation. Besides, it is assumed that for adjusting their path, dragonflies should see more neighbors as the optimization progresses. In fact, at the final optimization stage, to converge the optimum, the area of neighborhood increases and makes the swarm as a group. The best and worst solutions are considered as food and enemy.

A random walk (*Lévy* flight) is assumed to enhance the randomness, stochastic behavior and exploration phase when no neighboring solution can be found. Therefore, the following relation can be used to update the position:

$$X_{t+1} = X_t + Lévy(d) \times X_t \tag{B-8}$$

$$Lévy(x) = 0.01 \times \frac{r_1 \times \sigma}{|r_2|^{\frac{1}{\beta}}} \tag{B-9}$$

where d is the dimension of the position vector, r_1 and r_2 are two random numbers between 0 and 1, and σ can be estimated as follows:

$$\sigma = \left(\frac{\Gamma(1+\beta) \times \sin\left(\frac{\pi\beta}{2}\right)}{\Gamma(1+\beta) \times \beta \times 2^{\frac{\beta-1}{2}}} \right)^{1/\beta} \tag{B-10}$$

$$\Gamma(x) = (x-1)! \tag{B-11}$$

References:

[1] Artz J, Müller TE, Thenert K, Kleinekorte J, Meys R, Sternberg A, et al. Sustainable conversion of carbon dioxide: an integrated review of catalysis and life cycle assessment. Chem Rev 2018;118:434–504.
[2] Yang H, Zhang C, Gao P, Wang H, Li X, Zhong L, et al. A review of the catalytic hydrogenation of carbon dioxide into value-added hydrocarbons. Catal Sci Technol 2017;7:4580–98.
[3] Zhong J, Yang X, Wu Z, Liang B, Huang Y, Zhang T. State of the art and perspectives in heterogeneous catalysis of CO_2 hydrogenation to methanol. Chem Soc Rev 2020;49:1385–413.
[4] Marques Mota F, Kim DH. From CO_2 methanation to ambitious long-chain hydrocarbons: alternative fuels paving the path to sustainability. Chem Soc Rev 2019;48:205–59.
[5] Podrojková N, Sans V, Oriňak A, Oriňaková R. Recent developments in the modelling of heterogeneous catalysts for CO_2 conversion to chemicals. ChemCatChem 2020;12:1802–25.
[6] Kattel S, Liu P, Chen JG. Tuning selectivity of CO_2 hydrogenation reactions at the metal/oxide interface. J Am Chem Soc 2017;139:9739–54.
[7] Aresta M, Dibenedetto A, Angelini A. Catalysis for the valorization of exhaust carbon: from CO_2 to chemicals, materials, and fuels. technological use of CO_2. Chem Rev 2014;114:1709–42.
[8] Saeidi S, Amin NAS, Rahimpour MR. Hydrogenation of CO_2 to value-added products—a review and potential future developments. J CO_2 Util 2014;5:66–81.
[9] Landau M, Meiri N, Utsis N, Vidruk Nehemya R, Herskowitz M. Conversion of CO_2, CO, and H_2 in CO_2 hydrogenation to fungible liquid fuels on Fe-based catalysts. Ind Eng Chem Res 2017;56:13334–55.
[10] Saeidi S, Nikoo MK, Mirvakili A, Bahrani S, Amin NAS, Rahimpour MR. Recent advances in reactors for low-temperature Fischer-Tropsch synthesis: process intensification perspective. Rev Chem Eng 2015;31:209–38.
[11] Saeidi S, Fazlollahi F, Najari S, Iranshahi D, Klemeš JJ, Baxter LL. Hydrogen production: Perspectives, separation with special emphasis on kinetics of WGS reaction: a state-of-the-art review. J Ind Eng Chem 2017;49:1–25.
[12] Utsis N, Vidruk-Nehemya R, Landau M, Herskowitz M. Novel bifunctional catalysts based on crystalline multi-oxide matrices containing iron ions for CO_2 hydrogenation to liquid fuels and chemicals. Faraday Discuss 2016;188:545–63.
[13] Nikoo MK, Saeidi S, Lohi A. A comparative thermodynamic analysis and experimental studies on hydrogen synthesis by supercritical water gasification of glucose. Clean Technol Environ Policy 2015;17:2267–88.
[14] Saeidi S, Amiri MT, Amin NAS, Rahimpour MR. Progress in reactors for high-temperature Fischer-Tropsch process: determination place of intensifier reactor perspective. Int J Chem Reactor Eng 2014;12:639–64.
[15] Voitic G, Pichler B, Basile A, Iulianelli A, Malli K, Bock S, et al. Chapter 10 – hydrogen production. In: Hacker V, Mitsushima S, editors. Fuel Cells and Hydrogen. Elsevier; 2018. p. 215–41.
[16] Bičáková O, Straka P. Production of hydrogen from renewable resources and its effectiveness. Int J Hydrogen Energy 2012;37:11563–78.
[17] Acar C, Dincer I. Comparative assessment of hydrogen production methods from renewable and non-renewable sources. Int J Hydrogen Energy 2014;39:1–12.
[18] Najari S, Gróf G, Saeidi S. Enhancement of hydrogenation of CO_2 to hydrocarbons via In-Situ water removal. Int J Hydrogen Energy 2019;44:24759–81.
[19] Najari S, Gróf G, Saeidi S, Bihari P, Chen W-H. Modeling and statistical analysis of the three-side membrane reactor for the optimization of hydrocarbon production from CO_2 hydrogenation. Energy Convers Manage 2020;207:112481.
[20] Saeidi S, Najari S, Gróf G, Gallucci F. Effect of operating conditions and effectiveness factor on hydrogenation of CO_2 to hydrocarbons. Int J Hydrogen Energy 2019;44:28586–602.
[21] Liu M, Yi Y, Wang L, Guo H, Bogaerts A. Hydrogenation of carbon dioxide to value-added chemicals by heterogeneous catalysis and plasma catalysis. Catalysts 2019;9:275.
[22] Numpilai T, Chanlek N, Poo-Arporn Y, Cheng CK, Siri-Nguan N, Sornchamni T, et al. Tuning interactions of surface-adsorbed species over Fe− Co/K− Al_2O_3 catalyst by different K contents: selective CO_2 hydrogenation to light olefins. ChemCatChem 2020;12:3306–20.
[23] Numpilai T, Chanlek N, Poo-Arporn Y, Wannapaiboon S, Cheng CK, Siri-Nguan N, et al. Pore size effects on physicochemical properties of Fe-Co/K-Al_2O_3 catalysts and their catalytic activity in CO_2 hydrogenation to light olefins. Appl Surf Sci 2019;483:581–92.
[24] Gao P, Li S, Bu X, Dang S, Liu Z, Wang H, et al. Direct conversion of CO_2 into liquid fuels with high selectivity over a bifunctional catalyst. Nat Chem 2017;9:1019–24.
[25] Ra EC, Kim KY, Kim EH, Lee H, An K, Lee JS. Recycling carbon dioxide through catalytic hydrogenation: recent key developments and perspectives. ACS Catal 2020.
[26] Liu X, Wang M, Yin H, Hu J, Cheng K, Kang J, et al. Tandem catalysis for hydrogenation of CO and CO_2 to lower olefins with bifunctional catalysts composed of spinel oxide and SAPO-34. ACS Catal 2020;10:8303–14.
[27] Dokania A, Ramirez A, Bavykina A, Gascon J. Heterogeneous catalysis for the valorization of CO_2: role of bifunctional processes in the production of chemicals. ACS Energy Lett 2018;4:167–76.
[28] Shams K, Najari S. Dynamics of intraparticle desorption and chemical reaction in fixed-beds using inert core spherical particles. Chem Eng J 2011;172:500–6.
[29] Hartig F, Keil FJ. Large-scale spherical fixed bed reactors: modeling and optimization. Ind Eng Chem Res 1993;32:424–37.
[30] Hartig F, Keil F, Kafarov V. Optimization of Complex Reactions by Mixed-Integer Iterative Dynamic Programming. Theor Found Chem Eng 1995;30:50–60.
[31] Keil FJ, Rieckmann C. Optimization of three-dimensional catalyst pore structures. Chem Eng Sci 1994;49:4811–22.
[32] Iranshahi D, Hamedi N, Nategh M, Saeedi R, Saeidi S. Thermal integration of sulfuric acid and continuous catalyst regeneration of naphtha reforming plants. Chem Eng Technol 2018;41:637–55.
[33] Zhang L, Xia S, Chen L, Ge Y, Wang C, Feng H. Entropy generation rate minimization for hydrocarbon synthesis reactor from carbon dioxide and hydrogen. Int J Heat Mass Transf 2019;137:1112–23.
[34] Zhang L, Chen L, Xia S, Wang C, Sun F. Entropy generation minimization for reverse water gas shift (RWGS) reactors. Entropy 2018;20:415.
[35] Li P, Chen L, Xia S, Zhang L. Entropy generation rate minimization for methanol synthesis via a CO_2 hydrogenation reactor. Entropy 2019;21:174.
[36] Li P, Chen L, Xia S, Zhang L, Kong R, Ge Y, et al. Entropy generation rate minimization for steam methane reforming reactor heated by molten salt. Energy Rep 2020;6:685–97.
[37] Zhang L, Chen L, Xia S, Ge Y, Wang C, Feng H. Multi-objective optimization for helium-heated reverse water gas shift reactor by using NSGA-II. Int J Heat Mass Transf 2020;148:119025.
[38] Waldron C, Pankajakshan A, Quaglio M, Cao E, Galvanin F, Gavriilidis A. Model-based design of transient flow experiments for the identification of kinetic parameters. React Chem Eng 2020;5:112–23.
[39] Waldron C, Pankajakshan A, Quaglio M, Cao E, Galvanin F, Gavriilidis A. An autonomous microreactor platform for the rapid identification of kinetic models. React Chem Eng 2019;4:1623–36.
[40] Matera S, Schneider WF, Heyden A, Savara A. Progress in accurate chemical kinetic modeling, simulations, and parameter estimation for heterogeneous catalysis. ACS Catal 2019;9:6624–47.
[41] Berger RJ, Kapteijn F, Moulijn JA, Marin GB, De Wilde J, Olea M, et al. Dynamic methods for catalytic kinetics. Appl Catal A 2008;342:3–28.
[42] Slotboom Y, Bos M, Pieper J, Vrieswijk V, Likozar B, Kersten S, et al. Critical assessment of steady-state kinetic models for the synthesis of methanol over an industrial Cu/ZnO/Al_2O_3 catalyst. Chem Eng J 2020;389:124181.
[43] Seidel C, Jörke A, Vollbrecht B, Seidel-Morgenstern A, Kienle A. Kinetic modeling of methanol synthesis from renewable resources. Chem Eng Sci 2018;175:130–8.
[44] Saeidi S, Najari S, Fazlollahi F, Nikoo MK, Sefidkon F, Klemeš JJ, et al. Mechanisms and kinetics of CO_2 hydrogenation to value-added products: a detailed review on current status and future trends. Renew Sustain Energy Rev 2017;80:1292–311.
[45] Riedel T, Schaub G, Jun K-W, Lee K-W. Kinetics of CO_2 hydrogenation on a K-Promoted Fe Catalyst. Ind Eng Chem Res 2001;40:1355–63.
[46] Willauer HD, Ananth R, Olsen MT, Drab DM, Hardy DR, Williams FW. Modeling and kinetic analysis of CO_2 hydrogenation using a Mn and K-promoted Fe catalyst in a fixed-bed reactor. J CO_2 Util 2013;3–4:56–64.
[47] Kirsch H, Sommer U, Pfeifer P, Dittmeyer R. Power-to-fuel conversion based on reverse water-gas-shift, Fischer-Tropsch synthesis and hydrocracking: mathematical modeling and simulation in Matlab/Simulink. Chem Eng Sci 2020;227:115930.
[48] Sun C, Luo Z, Choudhary A, Pfeifer P, Dittmeyer R. Influence of the condensable hydrocarbons on an integrated Fischer-Tropsch synthesis and hydrocracking process: simulation and experimental validation. Ind Eng Chem Res 2017;56:13075–85.

[49] Do TN, Kim J. Green C_2–C_4 hydrocarbon production through direct CO_2 hydrogenation with renewable hydrogen: process development and techno-economic analysis. Energy Convers Manage 2020;214:112866.
[50] Najari S, Gróf G, Saeidi S, Gallucci F. Modeling and optimization of hydrogenation of CO_2: estimation of kinetic parameters via Artificial Bee Colony (ABC) and Differential Evolution (DE) algorithms. Int J Hydrogen Energy 2019;44:4630–49.
[51] Bonabeau E, Dorigo M, Theraulaz G. Swarm intelligence: from natural to artificial systems. Sante Fe Institute Studies in the Sciences of Complexity. Oxford University Press; 1999.
[52] Mirjalili S. Dragonfly algorithm: a new meta-heuristic optimization technique for solving single-objective, discrete, and multi-objective problems. Neural Comput Appl 2016;27:1053–73.
[53] Choi M-J, Kim J-S, Kim H-K, Lee S-B, Kang Y, Lee K-W. Hydrogenation of CO_2 over Fe-K based catalysts in a fixed bed reactors at elevated pressure. Korean J Chem Eng 2001;18:646–51.
[54] Kim J-S, Lee S, Lee S-B, Choi M-J, Lee K-W. Performance of catalytic reactors for the hydrogenation of CO_2 to hydrocarbons. Catal Today 2006;115:228–34.
[55] Lee S-B, Kim J-S, Lee W-Y, Lee K-W, Choi M-J. Product distribution analysis for catalytic reduction of CO_2 in a bench scale fixed bed reactor. In: Park S–E, Chang J–S, Lee K-W, editors. Studies in Surface Science and Catalysis, 153. Elsevier; 2004. p. 73–8.
[56] Lee S-C, Jang J-H, Lee B-Y, Kang M-C, Kang M, Choung S-J. The effect of binders on structure and chemical properties of Fe-K/γ-Al_2O_3 catalysts for CO_2 hydrogenation. Appl Catal A 2003;253:293–304.
[57] Riedel T, Claeys M, Schulz H, Schaub G, Nam S-S, Jun K-W, et al. Comparative study of Fischer-Tropsch synthesis with H_2/CO and H_2/CO_2 syngas using Fe- and Co-based catalysts. Appl Catal A 1999;186:201–13.
[58] Kim J-S, Lee S-B, Choi M-J, Kang Y, Lee K-W. Catalytic hydrogenation of carbon dioxide to light olefins in a fluidized bed reactor. In: Park S-E, Chang J-S, Lee K-W, editors. Studies in Surface Science and Catalysis, 153. Elsevier; 2004. p. 177–80.
[59] Kim JS, Kim HK, Lee SB, Choi MJ, Lee KW, Kang Y. Characteristics of carbon dioxide hydrogenation in a fluidized bed reactor. Korean J Chem Eng 2001;18:463–7.
[60] Iranshahi D, Golrokh A, Pourazadi E, Saeidi S, Gallucci F. Progress in spherical packed-bed reactors: Opportunities for refineries and chemical industries. Chem Eng Process-Process Intens 2018;132:16–24.
[61] Iranshahi D, Salimi P, Pourmand Z, Saeidi S, Klemeš JJ. Utilising a radial flow, spherical packed-bed reactor for auto thermal steam reforming of methane to achieve a high capacity of H_2 production. Chem Eng Process Process Intensif 2017;120:258–67.
[62] Chein R-Y, Yu C-T. Thermodynamic equilibrium analysis of water-gas shift reaction using syngases-effect of CO_2 and H_2S contents. Energy 2017;141:1004–18.
[63] Kaiser P, Unde RB, Kern C, Jess A. Production of liquid hydrocarbons with CO_2 as carbon source based on reverse water-gas shift and Fischer-Tropsch synthesis. Chem Ing Tech 2013;85:489–99.
[64] Shahhosseini HR, Saeidi S, Najari S, Gallucci F. Comparison of conventional and spherical reactor for the industrial auto-thermal reforming of methane to maximize synthesis gas and minimize CO_2. Int J Hydrogen Energy 2017;42:19798–809.
[65] Fernandez Rivas D, Boffito DC, Faria-Albanese J, Glassey J, Afraz N, Akse H, et al. Process intensification education contributes to sustainable development goals. Part 1. Educ Chem Eng 2020;32:1–14.
[66] Keil FJ. Process intensification. J Rev Chem Eng. 2018;34:135.
[67] Green DW, Perry RH. Perry's Chemical Engineers' Handbook/edición Don W. Green y Robert H. Perry; 1973.
[68] Lindsay AL, Bromley LA. Thermal conductivity of gas mixtures. Ind Eng Chem 1950;42:1508–11.
[69] Ghouse JH, Adams II TA. A multi-scale dynamic two-dimensional heterogeneous model for catalytic steam methane reforming reactors. Int J Hydrogen Energy 2013;38:9984–99.